

An overview of modelling of low-pressure post-discharge systems used for plasma sterilization

This article has been downloaded from IOPscience. Please scroll down to see the full text article.

2009 J. Phys.: Conf. Ser. 162 012008

(<http://iopscience.iop.org/1742-6596/162/1/012008>)

[The Table of Contents](#) and [more related content](#) is available

Download details:

IP Address: 148.6.27.69

The article was downloaded on 04/05/2009 at 10:19

Please note that [terms and conditions apply](#).

An overview of modelling of low-pressure post-discharge systems used for plasma sterilization

K Kutasi¹, C D Pintassilgo^{2,3}, J Loureiro²

¹ Research Institute for Solid State Physics and Optics of the Hungarian Academy of Sciences, POB 49, H-1525 Budapest, Hungary

² Instituto de Plasmas e Fusão Nuclear, Instituto Superior Técnico, 1049-001 Lisboa, Portugal

³ Departamento de Engenharia Física, Faculdade de Engenharia da Universidade do Porto, 4200-465 Porto, Portugal

E-mail: kutasi@mail.kfki.hu

Abstract. We present the modeling of a low pressure post-discharge system used for plasma sterilization, which consists of a flowing microwave discharge, an early-afterglow region developed downstream of the discharge in the same tube, and a large post-discharge reactor. The kinetic model valid for the discharge and early-afterglow region is based on the Boltzmann and rate balance equations, while in the post-discharge reactor a 3-D hydrodynamic model is used. The calculations are conducted in an N₂-O₂ mixture, which has seen to constitute an efficient system for sterilization purpose. The possibilities offered by modeling is presented through a discussion of the effects on relevant species densities and distributions caused by varying: (i) the initial gas mixture composition; (ii) the length of early-afterglow zone; (iii) the gas flow rate and gas pressure.

1. Introduction

In the last decade the use of polymer based heat sensitive tools in the medical praxis or pharmaceutical industry have brought the need of new low temperature sterilization and decontamination methods, which ensure complete inactivation or removal of all possible infectious microorganism: e.g. bacterial spores, viruses, or other potentially harmful biological residuals: e.g. endotoxins and proteins present on the used instruments. For the heat sensitive medical devices the most common sterilization methods in use are based on chemical treatment, which imply toxic active agents, or exposure to ionizing radiation, which may alter the bulk properties of polymers being sterilized.

A new method, which overcomes these drawbacks, implies the use of low-temperature plasmas. Low-temperature plasmas can be created either at atmospheric or low ($p \leq 10$ Torr) pressures. Numerous experimental studies have been carried out in different discharge configurations in a wide pressure range: i.e. atmospheric [1–15], mTorr [16–21] and Torr regions [22–29]; in various gas mixtures: e.g. N₂ [16, 18, 21], O₂ [13, 16, 18, 21], N₂-O₂ [7, 16, 21, 27, 30], Ar [6, 11, 14], Ar-O₂ [24], Ar-H₂ [19], O₂-H₂O [20], O₂-CF₄ [17], in order to test the sterilizing ability of these plasmas. Either the active discharge regions have been used [1, 8, 11, 16–19], or the afterglow region of discharges [7, 22, 24, 31]. *In this work we focus on the afterglow of low-pressure, Torr regime, discharges.*

Moreau *et al.* [22] have shown that total inactivation of an initial 10^6 spore (*Bacillus Subtilis*) population can be obtained using the flowing afterglow of a microwave discharge sustained in $N_2-2\%O_2$ at reduced gas pressure (typically 1–10 Torr). Moisan *et al.* [31] have shown that in these kind of afterglows the plasma sterilization can be explained by a synergistic effect between $O(^3P)$ atoms and UV photons emitted by $NO(B^2\Pi)$ molecules in the 250–320 nm spectral range (the so-called $NO\beta$ system). More recently, a detailed investigation of the UV spectrum correlated with the bacterial inactivation rate coefficient has shown that the $NO\gamma$ system (generated by $NO(A^2\Sigma^+)$), and not the $NO\beta$ system as stated in earlier publications, is the main UV photon contributor (Moisan *et al.* to be submitted, see also [32]). Philip *et al.* [25] state that the sterilization is the most efficient at the condition when the UV intensity is the highest, in their case at 2 Torr in $N_2-0.7\%O_2$, while Villeger *et al.* [27] have found the best sterilization condition when the O-atoms density is the highest and the UV radiation is still reasonably high, but not necessarily the highest, in their case at 5 Torr in $N_2-5\%O_2$. Nevertheless, the inactivation of spores have been also observed under very little or no UV radiation [33]. Furthermore, it has been shown that spores inactivation can be achieved also at 1-2 Torr in pure N_2 flowing afterglow due to the N atoms [34], which suggests that the N atoms present in an N_2-O_2 afterglow (where similar N densities can exist as in pure N_2) also contribute to sterilization [35]. Villeger *et al.* have shown that the N atoms can contribute to the sterilization through the temperature rise of the substrate induced by their recombination. Consequently, for an efficient sterilization large and homogeneous density distributions of N and O atoms, and $NO(A)$, $NO(B)$ molecules are necessary in a large volume reactor. Therefore, when analyzing the sterilization plasmas in order to define the sterilizing agents and to contribute to the optimization of the system it is important to determine the density distributions of these species in the reactor. The densities of the these species are influenced besides the discharge parameters, by the gas flow rate and gas pressure.

The densities of N and O atoms have been determined experimentally at various discharge conditions - by varying the gas pressure, gas flow rate and initial gas mixture composition - in the early-afterglow of a low-pressure N_2-O_2 post-discharge used for medical sterilization [24, 25, 27, 29, 36, 37]. The UV emission stemming from the $NO(B^2\Pi)$ upper state that yields photons over the $NO\beta$ bands (250-320 nm) has been registered in reactors (late-afterglow) for the same conditions [24, 25, 27, 29, 36]. The absolute N and O atoms densities are usually determined by NO titration in the early afterglow region, and therefore provide only the densities of atoms at the reactor's entrance. Boudam *et al.* [29] have determined the N atoms relative density in several positions in the reactor, mostly in the flow direction, with the Bockel's method [38], which is based on the intensity measurements at 580 nm of the first positive system ($N_2(B, v'=11)$). Here spatially integrated intensities are recorded, due to which a spatially averaged density is defined and thus the spatial inhomogeneity of the N atoms densities is masked. Contrary to this, the discharge modelling allows to obtain the density distributions of the various species present in the reactor, even of those whose densities cannot be measured experimentally. Calculations in post-discharge reactors used for surface treatments have been performed by Belmonte *et al.* [39]. Cylindrical reactors were modelled in $Ar-N_2(-H_2)$ [40] and $Ar-O_2(-H_2)$ [41] mixtures, used for nitriding and zirconia thin films deposition, respectively, with the help of the PHOENICS commercial code. The model gave as a result the density distributions of the species in the late post-discharge, however the initial densities at the beginning of the post discharge were not calculated accurately with a self consistent model.

In the sterilization chamber, besides the active species relevant for sterilization, there are also species, which may interact with the sterilized tools and induce damages. Some experimental works have reported the existence of a significant erosion of the spores and a variety of polymers in the afterglow chamber when the samples were located in the vicinity of the discharge tube axis [33]. In contrast, at a few cm away from the axis, no significant erosion has been observed

at low O₂ percentages. However, with increasing O₂ percentage the erosion appears, which according to Boudam *et al.* may be attributed to the enhancement of O-atoms density [29]. On the other hand, the strong on-axis erosion is suggested by the same authors [29] to be the action of the metastable state molecules: N₂(A), N₂(a'), and nitrogen molecular ions: N₂⁺, N₄⁺, species which characterize the so-called early afterglow. These facts draw another necessary condition to be satisfied by an optimal sterilizer, the reduction or elimination of the species believed to induce erosion from the reactor. This can be achieved by controlling the O₂ percentage in the initial gas mixture composition, the gas flow rate and the distance between the discharge and reactor. A self-consistent model of the discharge and of the early-afterglow allows the determination of the optimal discharge and geometrical parameters, where the above mentioned conditions are met.

Summarizing, the density distributions and the absolute densities of different species in the reactor can be controlled with: (i) the distance between the discharge and post-discharge reactor, as well as the geometry of this connecting tube, (ii) the discharge characteristics: tube radius, microwave field frequency, input power, (iii) the gas pressure, (iv) the initial gas mixture composition and (v) the gas flow rate. The density distributions of the species in the chamber can be also significantly influenced by the structure of the chamber, namely by the position of the inlets and outlets, which define the gas flow. The self-consistent model of the whole system makes it possible to investigate the effect of all these parameters on the density distributions of different species, as it will be presented in this paper.

The paper is structured as follows. In Section 2 the system set-up, while in the Section 3 the system's model is presented. The results are discussed in Section 4. Finally, the conclusions are drawn in Section 5.

2. System set-up

The system set-up, similar to the one used by the Montréal group in their experimental investigations [32], is shown in Figure 1. The surface-wave discharge is generated with a microwave field of 433 MHz, 915 MHz or 2450 MHz frequency in a tube of 0.6 cm inner diameter, which widens into a 2.6 cm inner diameter tube, that is connected to the reactor. During the calculations the tubes are assumed to be of variable lengths. The main frame of the parallelepipedic 50 L reactor, with dimensions of 60 cm×30 cm×28cm, is made of aluminium and is equipped with fused silica windows, which allows spectroscopic observations. The 2.6×2.6 cm² square inlet and outlet are located in the middle of the left side and bottom walls, respectively.

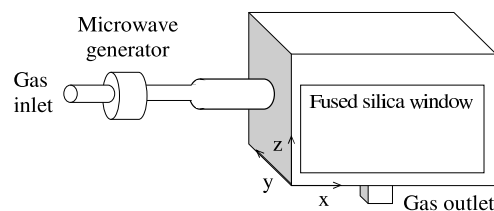


Figure 1. Post-discharge system.

3. Model

A post-discharge system has three main parts: (i) discharge region, (ii) early-afterglow region, which develops downstream from the discharge in the connecting tube between the discharge and the reactor and (iii) late afterglow present in the large volume reactor. The species created in the

discharge are carried by the gas flow through the early-afterglow region into the post-discharge reactor. In order to find out the species densities distribution in the post-discharge reactor, a self-consistent model of the whole system needs to be built up, which allows an accurate description of each section.

3.1. Discharge and early-afterglow model

The self-consistent model for the flowing microwave discharge is based on the solutions for the electron Boltzmann equation for the microwave field, coupled to a system of rate-balance equations for the neutral and charged heavy species [42]. Thus the electron energy distribution function (EEDF) is determined, and further the vibrational distribution functions (VDFs) of $N_2(X^1\Sigma_g^+, v)$ and $O_2(X^3\Sigma_g^-, v')$ molecules (with $0 \leq v \leq 45$ and $0 \leq v' \leq 15$), the concentrations of ground state $N(^4S)$ and $O(^3P)$; of the electronic states of molecular and atomic nitrogen and oxygen $N_2(A^3\Sigma_u^+, B^3\Pi_g, B'^3\Sigma_u^-, C^3\Pi_u, a'^1\Sigma_u^-, a^1\Pi_g, w^1\Delta_u)$ $O_2(a^1\Delta_g, b^1\Sigma_g^+)$ and $N(^2D, ^2P)$; the formed species $NO(X^2\Pi)$, $NO(A^2\Sigma^+)$, $NO(B^2\Pi)$, $NO_2(X,A)$ and O_3 ; the main positive ions $N_2^+(X^2\Sigma_g^+, B^2\Sigma_u^+)$, N_4^+ , O_2^+ , O^+ and NO^+ ; and negative ions O^- .

The reduced sustaining electric field in the plasma is self-consistently calculated by solving the continuity and transport equations for all these ionic species, including O^- , in order to describe the charged particle motion to the wall under the presence of a radial space-charge field. The reduced sustaining electric field in the plasma is determined using the requirement that under steady state conditions the total rate of ionization must compensate exactly for the rate of electron loss by electron-ion recombination plus ambipolar diffusion to the wall. It is worth to note here that this requirement ensures that the quasi-neutrality condition is obtained.

The model calculations have been performed for three typical laboratory conditions as follows: (i) $\omega/(2\pi) = 433$ MHz; (ii) $\omega/(2\pi) = 915$ MHz; (iii) $\omega/(2\pi) = 2450$ MHz. In a surface-wave discharge the electron density decreases from the excitation gap of the launcher to the plasma end, where the electron density reaches its cut-off value. In the case of surface wave mode propagation in a quartz tube, the critical electron densities associated with these frequencies are, respectively, $n_{ec} = 1.17 \times 10^{10} \text{ cm}^{-3}$, $5.20 \times 10^{10} \text{ cm}^{-3}$, and $3.74 \times 10^{11} \text{ cm}^{-3}$.

Since we analyse the early-afterglow downstream from the discharge, we only need to calculate the heavy-species concentrations in the plasma that correspond to a specific value of critical electron density. Within this approach, we obtain a set of initial solutions that is subsequently taken into account in a time-dependent system of master equations, where electronic processes are neglected. This formulation gives the temporal evolution of the populations in the early-afterglow.

The near afterglow that occurs downstream from the discharge, in the same discharge tube, has been considered by cutting-off the excitation by electron impact in the system of master equations. The time-dependent solutions obtained with this model constitute the initial conditions for the present 3D simulation.

3.2. Hydrodynamic model of the post-discharge reactor

The evolution of species densities in the reactor is described with a three dimensional hydrodynamic model. The model is composed of (i) the total mass conservation, (ii) the continuity equations for the different species (2), (iii) the total momentum conservation equation (3), and (iv) the total energy conservation equation (4). The gas is assumed to be a Newtonian fluid. The continuity equations can be written in the following form when the Soret and pressure diffusions are neglected, as well as the Dufour effect:

$$\int_S \rho \mathbf{v} \cdot \mathbf{n} dS = 0 \quad (1)$$

$$\int_S \rho y_k \mathbf{v} \cdot \mathbf{n} dS - \int_S \nabla(D_k \rho y_k) \cdot \mathbf{n} dS = \int_V m_k S_k^V dV + \int_S m_k S_k^S dS, \quad (2)$$

$$\int_S \rho u_i \mathbf{v} \cdot \mathbf{n} dS = \int_S \mu \text{grad } u_i \cdot \mathbf{n} dS - \int_S p \mathbf{i}_i \cdot \mathbf{n} dS. \quad (3)$$

$$\int_S \rho T \mathbf{v} \cdot \mathbf{n} dS = \int_S \frac{\lambda}{C_p} \text{grad } T \cdot \mathbf{n} dS \quad (4)$$

Here ρ denotes the total gas density, \mathbf{v} the gas velocity and \mathbf{n} the unit vector orthogonal to the S surface and directed outwards. Further, y_k denotes the relative mass density ($y_k = \rho_k / \rho$), D_k and m_k are the diffusion coefficient and the mass of the species k , and S_k^V and S_k^S represent the source terms associated with volume and surface reactions, respectively. Since S_k^S represents a term taking into account surface losses, this term is considered in (2) only on the last grid point at the proximity of the surface. u_i is the velocity in the i direction, p the static pressure, μ the dynamic viscosity, T is the gas temperature, C_p the specific heat at constant pressure and λ the thermal conductivity.

The term S_k^V is the sum of the source terms associated with the various gas phase reactions, which e.g. for a two body reaction has the form

$$S_{k,l}^V = k_{kl} n_k n_l, \quad (5)$$

with k_{kl} denoting the corresponding reaction rate coefficient, n_k and n_l the densities of species k and l involved in this particular reaction, with $n_k = y_k \rho / m_k$. The term for surface loss of the atomic species is calculated using the standard procedure

$$S_k^S = -\gamma_k \frac{v_k}{4} n_k, \quad (6)$$

where $v_k = \sqrt{8k_B T / \pi m_k}$ is the average velocity of k atoms and γ_k is the corresponding atomic surface loss probability. The γ surface loss probability includes all the possible surface reactions, thus it makes possible to describe the loss and creation of species on the surface without a detailed surface kinetic model.

In the afterglow the depopulation of the vibrational levels of the $N_2(X, v)$ ground state molecules and the charged species N_2^+ starts to take place. After a slight increase of the $N_2^+(X)$ and $N_2^+(B)$ ions population in the early-afterglow within the first 10 ms due to the V-V pumping-up mechanism [43], the population of the ions and of the high vibrational levels decrease fast, reaching very low densities in the late-afterglow, with no effect on the densities of most abundant species. Therefore, in the hydrodynamic model of the late afterglow we neglect several excited species and all the ions, which recombine in the early afterglow region, such as: the vibrational molecular distributions $N_2(X^1\Sigma_g^+, v)$ and $O_2(X^3\Sigma_g^-, v')$; the electronic states of molecular and atomic nitrogen $N_2(B^3\Pi_g, B'^3\Sigma_u^-, C^3\Pi_u, a'^1\Sigma_u^-, a^1\Pi_g, w^1\Delta_u)$ and $N(^2D, ^2P)$; the $NO_2(A)$ state; the main positive ions $N_2^+(X^2\Sigma_g^+, B^2\Sigma_u^+)$, N_4^+ , O_2^+ , O^+ and NO^+ ; and negative ions O^- . The set of gas phase reactions describing the kinetics of species as considered in the post-discharge chamber has been presented in [44] and [45]. The kinetic scheme for the creation of the $NO(A)$ and $NO(B)$ molecules has been recently revised and presented in [32].

The losses of atomic species on the wall are attributed to the NO formation on the wall and to the atomic re-association resulting in N_2 and O_2 , respectively, as presented in [46]. The surface losses of atomic species depend on many parameters, e.g. type of material, cleanliness, morphology, temperature, and surface coverage. In the literature it can be found numerous works dealing with the determination of the surface recombination probabilities of atoms (γ probabilities) for different materials, however, there is a quite large discrepancy between the results obtained by different authors, which could come from a particular surface treatment,

the purity of material, surface morphology, and surface properties like crystallinity, structure orientation, oxide or nitride type. The differences of several orders of magnitude found in certain cases may be also associated with the employment of different measuring techniques with different measurement errors. The atomic surface loss probability data are summarized in [46] for three different materials: Pyrex, aluminium and stainless steel.

The continuity equations are discretized using the finite volume method. The linear algebraic equation system so obtained is then solved with Stone's method iteratively using the multigrid method [47]. In our solution three grid levels are used, the finest grid has $80 \times 40 \times 40$ control volumes.

3.3. Validity of the models

The validity of the models have been shown in several publications by comparing the modeling results with the experimental one. In the discharge region, as presented in [48], the calculated O and O₂(a) densities were compared at different N₂ percentages in the N₂-O₂ mixture in the case of a discharge generated with 2450 MHz in a 16 mm diameter tube at 1 Torr pressure. The results illustrated in Figures 8 and 9 of [48] have shown a very good agreement between the calculated and experimental data, thus proved the correctness of the model and of the chosen kinetic scheme. The applicability of the early-afterglow model was shown in [44], where the calculated and measured densities of O atoms were compared at the reactor entrance in the afterglow of a discharge generated with 2450 MHz in a 26 mm diameter tube at 2 Torr pressure in N₂- $\chi\%$ O₂, with $\chi=1,2$; as illustrated in Figure 11 of [44].

The validity of the hydrodynamic model in the reactor has been examined by comparing, under different gas flow rates, the measured UV intensities with the calculated densities of the upper level of the related emitting species. Figure 9 in [32] shows a very good agreement between the measured UV intensity at 247.8 nm (band head of the NO(A² Σ^+ , v=0) to the NO(X² Π , v=2) transition) and the calculated NO(A) density along the reactor at a total pressure of 2 Torr and at three different N₂ gas flow rates: 400, 550 and 1000 sccm, when the O₂ gas flow rate is set at 8 sccm. The very good agreement found between the calculated and measured data indicates the excellent predicting capabilities of the model.

4. Results and discussion

4.1. Discharge and early-afterglow region

With the discharge model presented above it is possible to calculate the density of different species present in a microwave discharge along the discharge column. Since we are mainly interested in the afterglow, in the density of species leaving the discharge region, the calculations have been carried out only at the end of the discharge column, where the values of the electron density becomes equal to the critical density for surface wave mode propagation in a homogeneous, cold, collisionless plasma, surrounded by a dielectric. Here the species relative densities have been calculated for different discharge conditions by varying the (i) discharge tube radius, (ii) excitation field frequency, (iii) total gas pressure and (iv) initial gas mixture composition. These calculations make possible to choose those conditions where, from the application point of view, the optimal species densities are obtained. Here as an example we present the effect of the initial mixture composition on the species densities at the end of the discharge column.

Figure 2 shows the density of N(⁴S), O(³P), N₂(A), NO(X), NO(A) and NO(B) as a function of O₂% percentage in the N₂-O₂ initial gas mixture at 2 Torr pressure at the end of the discharge generated in a 0.6 cm diameter tube with 2450 MHz microwave field.

At low O₂ percentages the dominant atomic species in the N₂-O₂ discharges are the N(⁴S) atoms. At low pressures as 2 Torr, the N(⁴S) atoms are essentially created by direct electron impact dissociation on N₂(X ¹ Σ_g^+ , v) molecules. With increasing O₂ percentage in the mixture

the N atoms density decreases, now it is also controlled by the following populating and depopulating processes: $N_2(X, v \geq 13) + O \rightarrow N(^4S) + NO(X)$ and $N(^4S) + NO(X) \rightarrow N_2(X, v=3) + O$. However, due to a strong depopulation of $N_2(X, v \geq 13)$ levels by VT energy exchange reactions in collisions with $N(^4S)$ atoms at 2 Torr the main populating mechanism for $NO(X)$ is associated with the reaction $N_2(A) + O \rightarrow N(^2D) + NO(X)$. Due to the increase of O atoms density with O_2 percentage, the $NO(X)$ density also increases. The O atoms in the mixture are essentially produced via the reactions $N_2(B^3\Pi_g) + O_2(X^3\Sigma_g^-) \rightarrow N_2(X^1\Sigma_g^+, v=0) + O + O$ and $N(^4S) + NO(X) \rightarrow N_2(X^1\Sigma_g^+, v=3) + O$ and they are mainly lost by re-association on the wall of the discharge tube.

In the N_2 - O_2 mixture the UV emitting species are the $NO(A)$ and $NO(B)$ molecules, whose densities are order of magnitude lower than the atoms and $NO(X)$ densities. The densities of these two molecules behave similarly with the O_2 percentage, however the $NO(B)$ density is about three orders of magnitude lower than that of $NO(A)$. This difference can be understood from the analyses of the species populating and depopulating mechanisms. As a matter of fact, the $NO(A)$ state is exclusively populated by collisions of $N_2(A)$ with $NO(X)$: $N_2(A) + NO(X) \rightarrow N_2 + NO(A)$, whereas the destruction of this state occurs by radiative decay (99%), responsible for the emission of $NO\gamma$ system, and by quenching with O_2 and $NO(X)$, which contribution increases with pressure and with O_2 percentage. The production of $NO(B)$ takes place via the three-body mechanism $N(^4S) + O + (M) \rightarrow NO(B) + (M)$, with $M = (N_2, O_2)$, which in fact is not a single-stage process, since the recombination occurs firstly on a precursor state $NO(a^4\Pi)$ [32,49]. In what concerns the $NO(B)$ destruction, the radiative transfer to $NO(X)$ molecules, responsible for the emission of UV $NO\beta$ system, constitutes the main loss process.

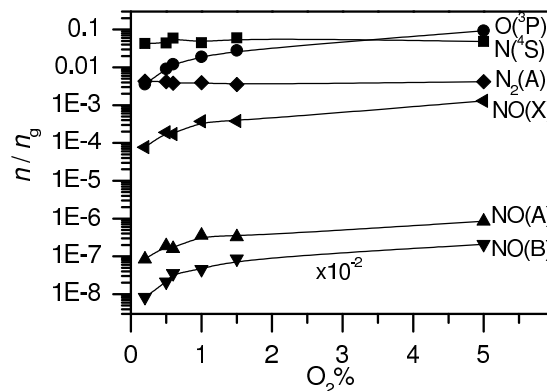


Figure 2. Calculated species densities (relative to gas density) at the end of the discharge column as a function of O_2 percentage added to N_2 at 2 Torr pressure and 2450 MHz excitation field frequency.

The early-afterglow model allows the study of the species densities evolution in time as they flow through the early-afterglow region, which develops downstream from the discharge in the connecting tube between the discharge and post-discharge reactor. In this region, since the excitation field is not present any more, the depopulation of the species starts to take place. The density of species entering the reactor can be controlled by varying the length of the connecting tube, which together with the applied gas flow determines the flight-time of species to the reactor entrance. In this way the density of species, which can cause damage to the treated materials can be minimized. In the following we examine the time evolution of the densities of the discharge effluents (ions and neutrals, metastable state species) as they enter the early-afterglow region and flow through it at 2 Torr with N_2 -1% O_2 initial mixture composition.

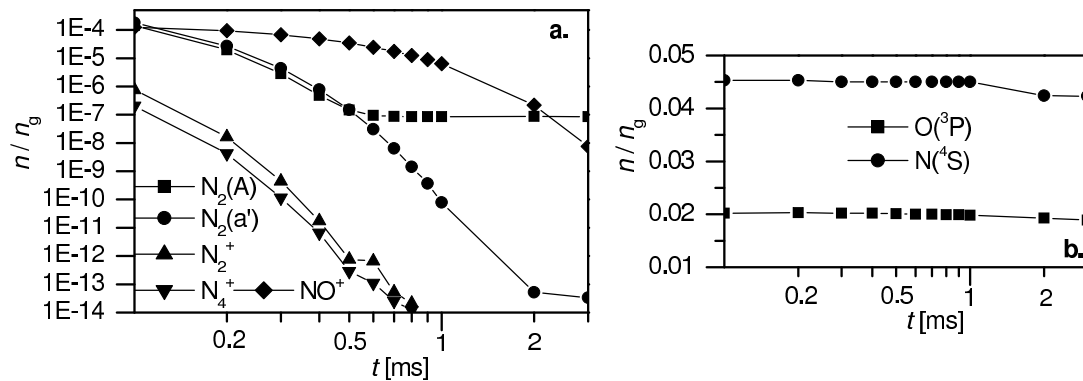


Figure 3. Time evolution of the densities (relative to gas density) of (a) metastables and ions, and (b) atoms at 2 Torr and 2450MHz with 1% O₂ added to N₂.

Figure 3(a) shows the time evolution of the densities of the ions and metastable molecules, which are believed to play a major role in the damage to materials exposed to plasma sterilization. The figure shows that the density of the N_2^+ and N_4^+ ions decreases by more than 8 orders of magnitude within 1 ms, reaching density values that ensure that no damage can result from these species. As far as the NO^+ ion is concerned, its density slightly increases initially, goes through a quasi plateau and then decreases slowly, ending at 2 ms with a value of 2 orders of magnitude lower than its initial one. The NO^+ is a long living ion, populated through the charge exchange of N^+ , O^+ , N_2^+ and O_2^+ in collision with neutral species. It is the dominating ion in an N₂-O₂ late afterglow [48]. In what concerns the metastable molecules, the density of $N_2(a')$ decreases by 10 orders of magnitude within 2 ms, whereas the density of $N_2(A)$ molecule, after an initial decrease by approximately 4 orders of magnitude over 0.5 ms, reaches a plateau that extends beyond at least 2 ms. The calculations have also shown that varying the O₂% from 0.2 to 2 the density of metastables and ions decrease faster except for the $N_2(A)$ and NO^+ (not shown in figure).

Figure 3(b) shows the time evolution in the early-afterglow of the relative densities of $O(^3P)$ and $N(^4S)$ atoms, which play important role in the sterilization process. The density of $O(^3P)$ does not vary during at least the first 3 ms, while the $N(^4S)$ density decreases, but barely, after 1 ms. We further note that, at 1%O₂, there is approximately two times more N than O atoms. The fact that N and O atom densities keep constant in the whole transition zone is strongly supported by the experiments where increasing the distance between the surfatron and the reactor from 3 cm to 10 cm show no significant changes in these densities (Boudam *et al.* [29], Figure 14). As already mentioned these atoms play also an important role in the NO(A) and NO(B) molecules formation. Figure 4 shows the time evolution of the NO(A) and NO(B) densities at 2 Torr with N₂-0.6%O₂ initial mixture composition. In the discharge, also shown by Figure 2, the density of NO(A) molecules dominates over that of NO(B), since here the NO(A) molecules are predominantly created by the two-body reaction of highly populated $N_2(A^3\Sigma_u^+)$ state with the NO($X^2\Pi$) ground state, while the NO(B) molecules are populated through a three-body re-association of N and O atoms. In contrast, in the early afterglow, as shown in Figure 4 the calculated relative density of the NO(A) molecules decreases markedly as a function of the species flight-time t (from $t = 0$ ms, the end of the discharge, to the beginning of the late afterglow), actually by three orders of magnitude during the first 0.2 ms. This can be explained by the decrease of the $N_2(A)$ state density with time in the early-afterglow, in fact according to the Figure 4 and Figure 3(a) the NO(A) and $N_2(A)$ densities decrease with approximately the same rate during this time period. As far as the density of the NO(B) state is concerned,

Figure 4 shows that it is constant throughout the early-afterglow time period examined. As a consequence of the strong decrease of the density of the NO(A) molecules during that time period, the density of the NO(B) state ends up approximately an order of magnitude higher than that of the NO(A) state after 0.4 ms and at least up to 1 ms, thereby setting the densities of NO(A) and NO(B) states at the very beginning of the late afterglow. Even that the density of NO(A) molecules is considerably lower in the afterglow than that of NO(B), since its radiation frequency is one order of magnitude higher than that of the NO(B), the contribution to the UV emission in the afterglow of both molecules is of the same order. As shown by Figure 4 after 0.4 ms the density of NO(A) and NO(B) molecules behave similarly, this occurs because here both molecules are predominantly created through the three-body re-association of N and O atoms, the only difference is that the two states are populated through different intermedial states, for the detailed kinetic scheme see [32].

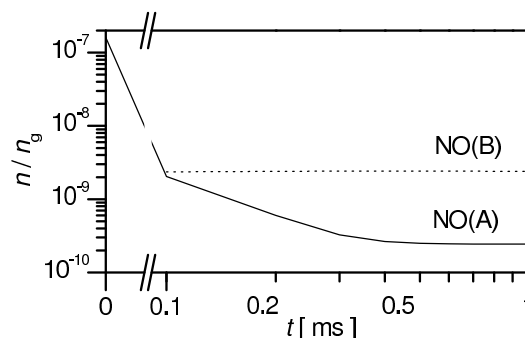


Figure 4. Calculated densities of UV emitting molecules as a function of the species flight-time in the early afterglow region, t .

4.2. Post-discharge region

The hydrodynamic model of the post-discharge reactor allows the calculation of the species densities distribution in the whole reactor. Here we present the effect of the gas flow rate applied and of the total gas pressure on the species density distributions.

4.2.1. Effect of the gas flow Figure 5 shows the calculated density distribution of NO(A), O(³P) and N(⁴S) states in the x - z vertical plane at $y=150$ mm (symmetry plane) at 2 Torr for N₂ flow rates of 400, 550 and 1000 sccm, with an O₂ flow rate set to 8 sccm. The first effect we can observe is that with gas flow the density distributions become more homogeneous, however due to the species different kinetics the distributions show different behaviours. At 400 sccm the NO(A) density decreases more than three orders of magnitude from the entrance to the opposite wall. This appears related to the corresponding decrease of the N and O atom densities, while the O atoms density decreases about one order of magnitude, the N atoms density is less with two orders of magnitude at the opposite wall comparing to the entrance. With increasing the gas flow rate the density distributions start to become more homogeneous. At 550 sccm the density decrease of the NO(A) molecules is about one order of magnitude in the reactor, similarly to that of the N atoms density, while the O atoms density decreases with about a factor of 2. In the case of a 1000 sccm gas flow, the O atoms density distribution is homogeneous in the whole reactor, while the NO(A) and N atoms densities vary just slightly in a significant part of the reactor. As already shown in the afterglow the NO(A) and NO(B) densities behave similarly, therefore the same distributions are obtained also for the NO(B) as for the NO(A), not shown

here in figure. The calculations also show that the density distribution of the UV emitting molecules is mostly determined by that of the N atoms.

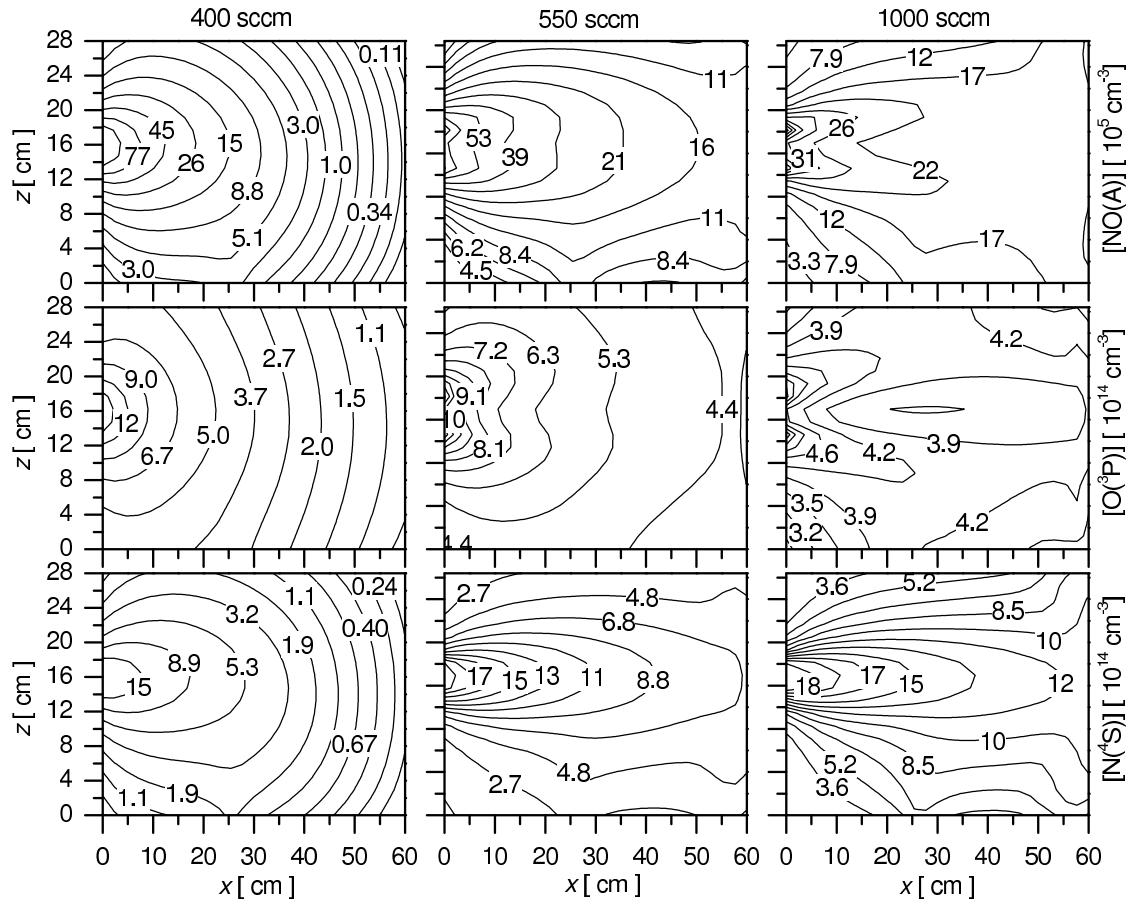


Figure 5. Calculated density distributions in the x - z plane at $y = 150$ mm in the reactor chamber at three N_2 gas flow rates with 8 sccm of O_2 added at a 2 Torr pressure and 2450 MHz field frequency. NO(A) (first row), $O(^3P)$ (second row) and $N(^4S)$ (third row). The densities are given in 10^5 cm^{-3} units for NO(A) and in 10^{14} cm^{-3} units for $O(^3P)$ and $N(^4S)$.

4.2.2. Effect of the total gas pressure Figure 6 provides spatially resolved density distribution of NO(A), $N(^4S)$ and $O(^3P)$ in the x - z symmetry plane at different pressure values at 1000 sccm N_2 and 8 sccm O_2 gas flow rates. It shows that uniformity of the species in the whole reactor volume is obtained only at the lowest pressure investigated, namely 2 Torr.

At 5 and 10 Torr, the density NO(A) state at the discharge (and flow) axis decreases only slightly, due to the high gas flow applied, but it decreases strongly when departing from the entrance axis. A closer look at the calculated NO(A) density at 10 Torr shows that at z positions different than that of the discharge axis, the lowest density can be found near the west wall, where the flow has no effect. The calculations for O and N atoms provide spatially resolved density distribution data, that are not easily accessible experimentally. These will help better understanding the observed spatial behaviour of the NO(A) density that depends on both the N and O atom density distribution. Figure 6 shows that the O-atom density increases with gas pressure but remains spatially almost uniform throughout the reactor chamber with

a slightly higher value along the flow. In contrast, the N-atom density for a given pressure value, is considerably higher at the axis and strongly decreases transversally to it the higher the pressure. The calculated spatial variations of the NO(A) density reflect the N-atom spatial density variations, and not those of O-atoms. In that respect, the stronger decrease of the N atom density with gas pressure is most probably due to reaction: $N(^4S) + N(^4S) + N_2 \rightarrow N_2(B) + N_2$, process that becomes more efficient with increasing pressure. The conclusion drawn from the calculations as concerns the respective role of N and O atoms on the emission intensity stemming from the NO(A) level is in agreement with the experimental data obtained for NO(B), see Figure 15 of Boudam *et al.* [29], which shows that the emission intensity follows the behaviour of N atoms and not that of the O atoms.

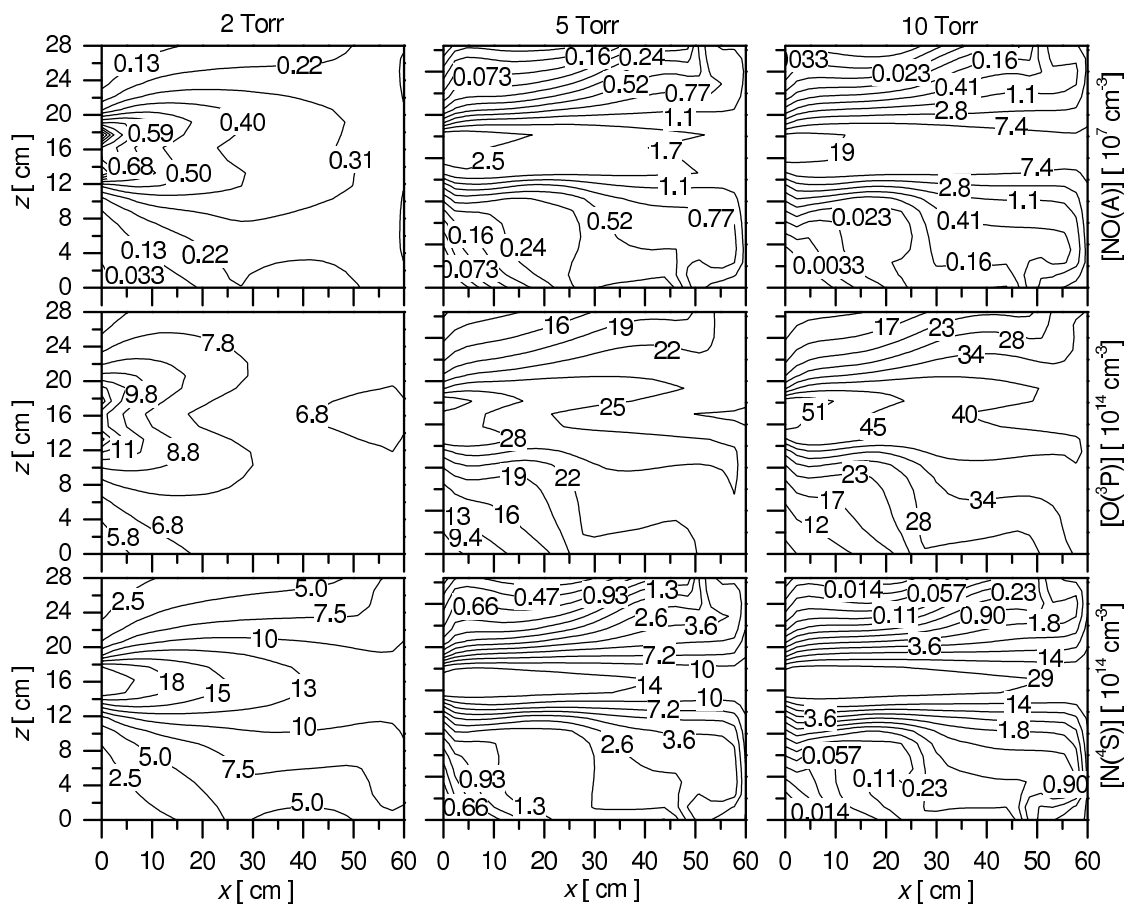


Figure 6. Calculated density distributions in the x - z plane at $y = 150$ mm in the reactor chamber at three gas pressure at a 1000 sccm N_2 flow rate and with 15 sccm of O_2 added (1.5%) at 2450 MHz. NO(A) (first row), $O(^3P)$ (second row) and $N(^4S)$ (third row). The densities are given in 10^7 cm^{-3} units for NO(A) and in 10^{14} cm^{-3} units for $O(^3P)$ and $N(^4S)$.

5. Conclusions

A low pressure post-discharge system used for plasma sterilization has been studied by means of modeling. The system investigated is composed of three parts: (i) a flowing microwave discharge, (ii) an early-afterglow region, which develops downstream after the end of the discharge in the same tube, and (iii) the late-afterglow region as a result of the entrance of the exit gas in a large

volume reactor. We have presented the models valid for these different regions: a kinetic model for the discharge and early-afterglow, and a 3-D hydrodynamic model for the post-discharge reactor. The application of the models have been illustrated with the N₂-O₂ system used for plasma sterilization.

In general trends, we have shown that the kinetic model allows for the possibility of calculating the species densities in the discharge and hence of choosing the best discharge conditions to obtain the required species densities at the end of the microwave discharge. With the kinetic model the time-evolution of the species densities in the early-afterglow can be obtained as well. By modeling it makes possible to determine the optimal length of the connecting tube between the discharge tube and the post-discharge reactor for every discharge condition. This study allows to avoid that the species able to damage the material to be sterilized may enter the reactor, whereas the species playing a role in the sterilization process remain with high enough concentrations. Furthermore, we have shown that with the help of the 3-D hydrodynamic model some important discharge parameters, such as the total gas pressure and gas flow rate can be adjusted in a way that the density distributions of the relevant species for sterilization to be homogeneous in the reactor. We have demonstrated that the modeling is a useful tool for optimizing the post-discharge systems used for plasma sterilization.

Our calculations have shown that in order to achieve a homogeneous density distribution of N and O atoms, and of UV emitting NO(A) and NO(B) molecules in the whole reactor pressures as low as 2 Torr should be used and gas flows as high as 1000 sccm. If the entry of the ions into reactor is aimed to be avoided the connecting tube between the discharge and reactor should be designed in the way to assure that the species flight-time in this region is at least 1 ms.

Acknowledgments

The work has been supported by the Hungarian Science Foundation OTKA through F-67556 and by Portuguese Science Foundation FCT. The authors gratefully acknowledge Professor Michel Moisan and Dr. Bachir Saoudi for several fruitful discussions.

References

- [1] Kelly-Wintenberg K, Montie T C, Brickman C, Roth J R, Carr A K, Sorge K, Wadsworth L C, Tsai P P Y 1998 *J. Ind. Microbiology. and Biotechnology* **20** 69
- [2] Herrmann H W, Henins I, Park J, Selwyn G S 1999 *Physics of Plasmas* **6** 2284
- [3] Roth J R, Sherman D M, Gadri R B, Karakaya F, Chen Z, Montie T C, Kelly-Wintenberg K 2000 *IEEE Trans. Plasma. Sci.* **28** 56
- [4] Laroussi M 2002 *IEEE Trans. Plasma Sci.* **30** 1409
- [5] Heise M, Neff W, Franken O, Muranyi P, Wunderlich J 2004 *Plasmas and Polymers* **9** 23
- [6] Lee K-Y, Park B J, Lee D H, Lee I-S, Hyun S O, Chung K-H, Park J-C 2005 *Surf. Coat. Technol.* **193** 35
- [7] Pointu A M, Ricard A, Dodet B, Odic E, Larbre J and Ganciu M 2005 *J. Phys. D: Appl. Phys.* **38** 1905
- [8] Ohkawa H, Akitsu T, Tsuji M, Kimura H, Fukushima K 2005 *Plasma Processes and Polymers* **2** 120
- [9] Boudam M K, Moisan M, Saoudi B, Popovici C, Gherardi N and Massines F 2006 *J. Phys. D: Appl. Phys.* **39** 3494
- [10] Sato T, Fujioka K, Ramasamy R, Urayama T, Fujii S 2006 *IEEE Trans. On Industry Applications* **42** 399 (2006)
- [11] Yu Q S, Huang C, Hsieh F H, Huff H, Duan Y 2006 *Appl. Phys. Lett.* **88** 013903
- [12] Fridman G, Peddinghaus M, Ayan H, Fridman A, Balasubramanian M, Gutsol A, Brooks A, Fridman G 2006 *Plasma Chem. Plasma Process.* **26** 425
- [13] Lee K et al. 2006 *J. Microbiology* **44** 269
- [14] Park B J, Lee D H, Park J-C, Lee I-S, Lee K-Y, Hyun S O, Chun M S, Chung K H 2007 *Surf. Coat. Technol.* **201** 5738
- [15] Puać N, Petrović Z Lj, Malović G, Djordjević A, Zivković S, Giba Z, Grubisic D 2006 *J. Phys. D: Appl. Phys.* **39** 3514
- [16] Feichtinger J, Schulz A, Walker M, Schumacher U 2003 *Surf. Coat. Technol.* **174-175** 564
- [17] Lerouge S, Wertheimer M R, Marchand R, Tabrizian M, Yahia L'H 2000 *J Biomed Mater Res.* **51** 128
- [18] Nagatsu M, Terashita F, Nonaka H, Xu L, Nagata T, Koide Y 2005 *Appl. Phys. Lett.* **86** 211502

- [19] Rossi F, Kylian O, Hasiwa M 2006 *Plasma Process. Polym.* **3** 431
- [20] Hayashi N, Guan W, Tsutsui S, Tomari T, Hanada Y 2006 *Jpn. J. Appl. Phys.* **45** 8358
- [21] Xu L, Nonaka H, Zhou H Y, Ogino A, Nagata T, Koide Y, Nanko S, Kurakawi I, Nagatsu M 2007 *J. Phys. D: Appl. Phys.* **40** 803
- [22] Moreau S, Moisan M, Tabrizian M, Barbeau J, Pelletier J, Ricard A, Yahia L'H 2000 *J. Appl. Phys.* **88** 1166
- [23] Lerouge S, Fozza A C, Wertheimer M R, Marchand R, Yahia L'H 2000 *Plasmas and Polymers* **5** 31
- [24] Ricard A, Moisan M and Moreau S 2001 *J. Phys. D: Appl. Phys.* **34** 1203
- [25] Philip N, B. Saoudi, M-Ch. Crevier, M. Moisan, J. Barbeau, J. Pelletier 2002 *IEEE Trans. Plasma Sci.* **30** 1429
- [26] Monna V, Nguyen C, Kahil M, Ricard A, Sixou M 2000 *IEEE Trans. Plasma Sci.* **30** 1437
- [27] Villegier S, Cousty S, Ricard A and Sixou M 2003 *J. Phys. D: Appl. Phys.* **36** L60
- [28] Laroussi M 2005 *Plasma Processes and Polymers* **2** 391
- [29] Boudam M K, Saoudi B, Moisan M, Ricard A 2007 *J. Phys. D: Appl. Phys.* **40** 1694
- [30] Kylian O, Sasaki T, Rossi F 2006 *Eur. Phys. J. Appl. Phys.* **34** 139
- [31] Moisan M, Barbeau J, Crevier M-Ch, Pelletier J, Philip N, Saoudi B 2002 *Pure Appl. Chem.* **74** 349
- [32] Kutasi K, Saoudi B, Pintassilgo C D, Loureiro J, Moisan M 2008 *Plasma Process. Polym.* **5** 840
- [33] Crevier M C, Moisan M, Yahia L, Saoudi B 2002 Proc. Int. Symp. on Advanced Materials for Biomedical Applications (SAMBA) (Montreal, Quebec) 365
- [34] Cousty S, Villegier S, Sarette J P, Ricard A, Sixou M 2006 *Eur. Phys. J. Appl. Phys.* **34** 143.
- [35] Villegier S, Cousty S, Ricard A 2005 *Plasma Process. Polym.* **2** 709
- [36] Ricard A and Monna V 2002 *Plasma Sources Sci. Technol.* **11** 1
- [37] Ricard A, Monna V and Mozetic M 2003 *Surf. Coat. Technol.* **174-175** 905
- [38] Bockel S, Damiy A M, Ricard A 1995 *Surf. Coat. Technol.* **74-5** 474
- [39] Belmonte T, Czerwiec T, Michel H 2001 *Surf. Coat. Technol.* **142-144** 306
- [40] Belmonte T, Jaoul C, Borges J N 2004 *Surface Coat. Technol.* **188-189** 201
- [41] Belmonte T, Czerwiec T, Garvillet J, Michel H 1997 *Surface Coat. Technol.* **97** 642
- [42] Pintassilgo C D, Loureiro J, Guerra V 2005 *J. Phys. D: Appl. Phys.* **38** 417
- [43] Sá P A, Guerra V, Loureiro J, Sadeghi N 2004 *J. Phys. D: Appl. Phys.* **37** 221
- [44] Kutasi K, Pintassilgo C D, Coelho P J, Loureiro J 2006 *J. Phys. D: Appl. Phys.* **39** 3978
- [45] Kutasi K, Pintassilgo C D, Loureiro J, Coelho P J 2007 *J. Phys. D: Appl. Phys.* **40** 1990
- [46] Kutasi K, Loureiro J 2007 *J. Phys. D: Appl. Phys.* **40** 5612
- [47] Ferziger J H and Peric M *Computational Methods for Fluid Dynamics* 2002, 3rd rev. ed., Springer
- [48] Guerra V, Loureiro J 1999 *Plasma Sources Sci. Technol.* **8** 110
- [49] Gross R W and Cohen N 1968 *J. Chem. Phys.* **48** 2582